

Modeling Magma Dynamics with a Mixed Fourier Collocation — Discontinuous Galerkin Method

Alan R. Schiemenz^{1,2,*†}, Marc A. Hesse³ and Jan S. Hesthaven²

¹ Department of Geological Sciences, Brown University, Providence, RI 02910, USA.

² Division of Applied Mathematics, Brown University, Providence, RI 02910, USA.

³ Department of Geological Sciences, University of Texas at Austin, Austin, TX 78712, USA.

Received 3 February 2010; Accepted (in revised version) 24 September 2010

Available online 28 April 2011

Abstract. A high-order discretization consisting of a tensor product of the Fourier collocation and discontinuous Galerkin methods is presented for numerical modeling of magma dynamics. The physical model is an advection-reaction type system consisting of two hyperbolic equations and one elliptic equation. The high-order solution basis allows for accurate and efficient representation of compaction-dissolution waves that are predicted from linear theory. The discontinuous Galerkin method provides a robust and efficient solution to the eigenvalue problem formed by linear stability analysis of the physical system. New insights into the processes of melt generation and segregation, such as melt channel bifurcation, are revealed from two-dimensional time-dependent simulations.

AMS subject classifications: 65Z05, 65M22, 65M70, 65T40, 65T50

Key words: Magma dynamics, discontinuous Galerkin method, Fourier collocation method, numerical simulations, linear stability analysis.

1 Introduction

Within the mantle of the Earth, melt is spontaneously generated and then segregated from its source, migrating upwards towards the Earth's surface. Melt is generated by adiabatic decompressional melting during upwelling in the Earth's upper mantle. Segregation of melt involves two-phase flow in which low viscosity melt percolates through a much more viscous solid matrix [3]. During its upward migration, melt generated in the

*Corresponding author. *Email addresses:* alan.schiemenz@geophysik.uni-muenchen.de (A. R. Schiemenz), mhesse@jsg.utexas.edu (M. A. Hesse), Jan.Hesthaven@brown.edu (J. S. Hesthaven)

†Current address: Department of Earth and Environmental Sciences, Geophysics, Munich University, Theresienstr. 41, 80333 Munich, Germany.

deeper part of the upwelling mantle will interact both thermally and chemically with the overlying mantle. Our understanding of the evolution of melt is constrained by physical evidence based upon field observations at ophiolites, where sections of the Earth's mantle have been uplifted and exposed at the surface. The key observation from these outcrops is the local depletion of a soluble mineral, orthopyroxene (opx). This observation has been interpreted as the localization of porous melt flow into high porosity melt channels that have led to the depletion of the soluble mineral. The main objective of the present study is to develop a high-order numerical model that can be used to study the interaction between the melt and solid mantle during melt migration. Unlike previous studies we explicitly track the evolution of the soluble mineral (opx) to understand the formation of the observed opx-depletions and their spatial and temporal relation to localized melt flow in regions of high permeability.

A fundamental geologic observation that gives insight into the existing theory of melt transport is that the chemical composition of erupted basalt is not in equilibrium with residual mantle at low pressure, particularly at diverging plate boundaries. Additionally, it is observed that the mantle is chemically and lithologically heterogeneous. To preserve the geochemical signature developed at depth, melt must rise from depths of at least 30 km to the surface without extensive re-equilibration with the surrounding mantle. One mechanism for this involves reactive infiltration instability, where highly porous regions form due to a feedback between melt flow and dissolution of a soluble mineral in the solid. It has been suggested that high-permeability dunite channels act as conduits for focused flow, where melt may efficiently segregate from its source region while still maintaining its geochemical signature at depth. For further discussion we refer to [9] and the references therein.

Previous numerical study utilizing a low-order finite difference scheme was presented in [13], and demonstrated localization of the melt flow into high-porosity channels. However, this work does not explicitly account for the soluble mineral opx, whose presence is integral to the formation of dunite channels, nor does it consider the effects of upwelling or a bulk viscosity dependent upon the porosity. Further numerical study incorporating upwelling of the mantle was given in [12], although this work does not discuss the numerical model used. In this paper, a high-order accurate numerical model is presented following the physical models presented in [6, 11], which include upwelling, a porosity-dependent bulk viscosity, and an additional equation to track the opx abundance. We assume a formulation of local chemical equilibrium with negligible diffusion in the melt. Linear analysis of our system predicts the emergence of compaction-porosity waves; in addition to the balancing between upwelling, dissolution and compaction, these features present a formidable challenge in numerical modeling. We address this challenge by developing a high-order numerical method that provides accurate resolution at a reasonable cost. Numerical simulations confirm the existence of compaction-porosity waves, and also demonstrate that melt channels are not necessarily spatially or temporally correlated with dunite channels.

This paper is organized as follows. In Section 2 we detail the non-dimensionalized

governing equations. In Section 3 we present a high-order numerical discretization consisting of a discontinuous Galerkin scheme in the vertical dimension and a Fourier collocation scheme in the horizontal dimension. In Section 4 we perform a linear stability analysis of the physical model, and show that results from transient numerical simulations match what is predicted from the linear stability analysis. In Section 5 we present two-dimensional results from transient numerical simulations under varying initial and inflow boundary conditions in porosity.

2 Physical model

The governing equations for our model system have been previously discussed in [1, 13], and later extended in [6, 11] to incorporate upwelling, porosity-dependent bulk viscosity, and explicit tracking of opx. A reactive time scale was used in [6], whereas an upwelling time scale was used in [11]. Below we present the non-dimensionalized equations on a reactive time scale; we refer to [6, 11] for details of the non-dimensionalization and scaling.

We consider a three-phase system with an interconnected melt or fluid phase and a solid matrix, comprising an insoluble mineral, olivine (ol), and a soluble mineral, opx. The evolution of the melt fraction, ϕ_f , is given as the conservation law

$$\frac{\partial \phi_f}{\partial t} = -\frac{\gamma}{\delta} \frac{\partial \phi_f}{\partial z} + p\phi_f + \Gamma_{opx}. \quad (2.1)$$

The three right-hand-side terms of Eq. (2.1) represent upwelling, compaction, and dissolution, respectively. Upwelling is the gradual rise of the Earth's mantle in the positive z (upwards) direction. Compaction is the volume change of the solid matrix. Dissolution is the process by which opx is converted to melt. Together the three processes effectively form an advection-reaction type equation. Eq. (2.1) contains the dimensionless parameters δ , representing the solubility gradient of the equilibrium concentration of the soluble mineral in the fluid, and γ , representing the ratio of the solid upwelling to the melt buoyancy.

Similar to Eq. (2.1), the evolution of the opx abundance, ϕ_{opx} , is given as the conservation law

$$\frac{\partial \phi_{opx}}{\partial t} = -\frac{\gamma}{\delta} \frac{\partial \phi_{opx}}{\partial z} - \varphi \Gamma_{opx}. \quad (2.2)$$

Here, φ is the mantle fertility rate, effectively representing the rate at which opx is consumed in the dissolution process. Hence, the dissolution term in Eq. (2.2) carries an opposite sign as in Eq. (2.1); the former represents depletion of opx whereas the latter represents generation of melt. Darcy's law yields the fluid velocity \mathbf{v} relative to the uniform solid upwelling via the algebraic equation

$$\phi_f \mathbf{v} - \gamma \phi_f \mathbf{n}_z = -\phi_f^3 (\delta \nabla p - \mathbf{n}_z), \quad (2.3)$$

where \mathbf{n}_z is the unit vector in the vertical dimension. Coupling Darcy's law to momentum conservation, the following elliptic equation is derived for the fluid-solid pressure difference p ,

$$-\nabla \cdot [\delta\phi_f^3 \nabla p] + \delta p \phi_f = -\frac{\partial \phi_f^3}{\partial z}. \tag{2.4}$$

Finally, the dissolution rate, Γ_{opx} , is proportional to the Darcy flux, $\phi_f \mathbf{v}$, and is computed algebraically as

$$\begin{aligned} \Gamma_{opx} &= \frac{\phi_f (\mathbf{v} \cdot \mathbf{n}_z)}{1 - \delta z} \mathcal{I}_{\phi_{opx}} \\ &= \frac{1}{1 - \delta z} \left(\gamma \phi_f - \delta \phi_f^3 \frac{\partial p}{\partial z} + \phi_f^3 \right) \mathcal{I}_{\phi_{opx}}, \end{aligned} \tag{2.5}$$

where the indicator function $\mathcal{I}_{\phi_{opx}} = \mathcal{I}_{\phi_{opx}}(x, z)$ returns 1 if ϕ_{opx} is positive and zero otherwise. In this way, dissolution occurs only if the soluble mineral opx is present. We assume periodicity in the horizontal dimension, whereas boundary conditions in the vertical dimension are given as

$$\phi_f(x, 0, t) = 1, \quad \phi_{opx}(x, 0, t) = 1, \tag{2.6a}$$

$$p(x, 0, t) = -1 - \gamma, \quad \frac{\partial p}{\partial z}(x, z_{\max}, t) = 0. \tag{2.6b}$$

The initial-boundary value problem (2.1)-(2.6) contains the dimensionless parameters δ , γ , and φ . Unless otherwise noted, we choose standard values for these parameters to be

$$\delta = 10^{-2}, \quad \gamma = 10^{-2}, \quad \varphi = 0.266. \tag{2.7}$$

Assuming a positive opx abundance, dissolution is nonzero and one-dimensional analysis [6] of the system (2.1)-(2.6) yields the approximate steady states

$$\bar{\phi}_f = \left(1 + q_0 \frac{\delta z}{1 - \delta z} \right)^{1/3}, \tag{2.8a}$$

$$\bar{\phi}_{opx} = 1 - \frac{\varphi q_0}{\gamma} \frac{\delta z}{1 - \delta z}, \tag{2.8b}$$

$$\bar{p} = -\frac{q_0}{(1 - \delta z)^2}, \tag{2.8c}$$

where $q_0 = 1 + \gamma$. Solving for $\bar{\phi}_{opx} = 0$, the location of opx exhaustion, z^* , is

$$z^* = \frac{\gamma / \delta}{\varphi q_0 + \gamma}. \tag{2.9}$$

As the dissolution rate is everywhere zero at heights greater than z^* , z^* is a natural upper bound on the column height z_{\max} . Beyond this restriction, z_{\max} is not precisely constrained. In [11], it is shown that taking a shorter (vertically) domain while fixing all other

parameters enlarges the stable regime of parameter space. In this work we will choose the column height to be 75% of the opx exhaustion height,

$$z_{\max} = 0.75z^*. \quad (2.10)$$

For the parameter selections (2.7) this yields $z_{\max} \approx 2.69$.

3 Numerical discretization

To solve the system (2.1)-(2.6) we employ a nodal discontinuous Galerkin (DG) scheme [8] in the vertical dimension and a Fourier collocation (FC) scheme [7], also known as a pseudospectral scheme, in the horizontal dimension. Time is discretized with an explicit, fourth-order Runge-Kutta (RK) scheme. The rationale behind these choices are as follows. The high-order nature of the spatial discretization provides the necessary accuracy to efficiently resolve the dynamics of the problem, which involves a balance of upwelling, compaction and dissolution. Linear stability analysis of the physical system ([6]; see also Section 4 below) predicts the emergence of compaction-dissolution waves, for which a high-order approach is well-suited to resolve. The assumption of periodic boundary conditions in the horizontal direction is easily satisfied by the FC scheme, where solutions are represented by periodic basis functions. An explicit method is sufficient for time stepping and simple to implement, requiring only function evaluations of the non-linear right-hand-sides to (2.1)-(2.2). Unlike previous numerical studies [13], our model assumes local chemical equilibrium and thus explicit time stepping is not restricted by a large reaction rate constant. The terms limiting time integration therefore are the upwelling and dissolution terms in (2.1) and are typically of comparable magnitude.

Proceeding by a method-of-lines approach, the spatial operations in the hyperbolic equations (2.1)-(2.2) are discretized to produce a system of differential-algebraic equations that are a function of time only. Time integration is performed with the five-stage, fourth-order RK method as detailed in [5]. Each inner RK stage is concluded by discretizing the elliptic equation (2.4) with the updated value of ϕ_f ; we use an iterative method to solve for p in the resulting linear system.

3.1 Selecting a mesh

Before detailing the numerical schemes we first introduce a mesh,

$$(x_i, z_j^k) \in X \times Z. \quad (3.1)$$

An even number M of equidistant horizontal points are chosen,

$$X = \{0 = x_0, x_1, \dots, x_{M-1}\}, \quad x_i = \frac{i}{M}x_{\max}. \quad (3.2)$$

These grid points yield the explicitly defined interpolating polynomials l_i^{FS} ,

$$l_i^{FS}(x) = \frac{1}{M} \sin \left[\frac{\pi M}{x_{\max}} (x - x_i) \right] \cot \left[\frac{\pi}{x_{\max}} (x - x_i) \right], \tag{3.3}$$

as well as the discrete differentiation operator [7]

$$(\mathcal{D}^x)_{ij} = \left. \frac{d}{dx} l_j^{FS}(x) \right|_{x_i} = \begin{cases} (-1)^{i+j} \frac{\pi}{x_{\max}} \cot \left[\frac{\pi}{x_{\max}} (x_i - x_j) \right], & i \neq j, \\ 0, & i = j. \end{cases} \tag{3.4}$$

Defining the vertical grid points $z_k^k \in Z$ requires more effort. Z is comprised of K (interval) elements I^k ,

$$Z = \bigcup_{k=1}^K I^k, \quad I^k = \{z_0^k, z_1^k, \dots, z_N^k\}, \tag{3.5}$$

where the value chosen for N determines the local order of approximation. For each element a set of grid points is introduced,

$$z_N^{k-1} = z_0^k < z_1^k < \dots < z_N^k = z_0^{k+1}, \quad z_N^0 = 0, z_0^{K+1} = z_{\max}. \tag{3.6}$$

It is noted that at cell boundaries the solution is doubly-defined. Although in theory any choice of grid points may suffice, in practice one would prefer a set that is optimal for computation. In particular, for higher N the choice of equidistant grid points leads to poorly conditioned operators. Instead, we use the Gauss-Lobatto points which lead to well-conditioned operators. While these points cannot be defined explicitly, they can be computed in a pre-processing step; see [8] for an efficient implementation in MATLAB. Similar to the notation (3.3)-(3.4) introduced for the FC scheme, we define interpolating polynomials $l_j^{DG,k}$ on the grid points (3.6) and a corresponding differentiation matrix

$$(\mathcal{D}^{z,k})_{m,n} = \left. \frac{dl_n^{DG,k}}{dz} \right|_{z=z_m^k}, \quad 0 \leq m, n \leq N. \tag{3.7}$$

With the mesh defined by (3.1), the solution variables $u \in \{\phi_f, \phi_{opx}, p\}$ are discretized as

$$u \simeq u_h = \bigoplus_{k=1}^K u_h^k(x, z, t), \quad u_h^k(x, z, t) = \sum_{i=0}^{M-1} \sum_{j=0}^N u_h^k(x_i, z_j^k) l_i^{FS}(x) l_j^{DG,k}(z). \tag{3.8}$$

On the rectangular patch $X \times I^k$, representing the entire domain width and vertical section corresponding to DG element k , solutions are represented as the two-dimensional array

$$u_h^k(x, z, t) = \begin{bmatrix} u_{0,0}^k & u_{0,1}^k & \dots & u_{0,M-1}^k \\ u_{1,0}^k & u_{1,1}^k & \dots & u_{1,M-1}^k \\ \vdots & \vdots & \dots & \vdots \\ u_{N,0}^k & u_{N,1}^k & \dots & u_{N,M-1}^k \end{bmatrix}, \tag{3.9}$$

where $u_{j,i}^k = u_h^k(x_i, z_j^k, t)$. Therefore, discrete z operators act on columns from the left while x operators act on rows from the right.

3.2 Full numerical method

Having defined a mesh, the full numerical method is detailed, beginning with the porosity evolution (2.1). Evolution of opx abundance (2.2) and compaction rate (2.4) follow thereafter. On the rectangular patch $X \times I^k$, the residual R_h^k is formed by substituting the numerical solutions

$$u_h^k = \left\{ (\phi_f)_h^k, (\phi_{opx})_h^k, p_h^k \right\} \quad (3.10)$$

into (2.1),

$$R_h^k(x, z, t) = \frac{\partial (\phi_f)_h^k}{\partial t} + \frac{\gamma}{\delta} \frac{\partial (\phi_f)_h^k}{\partial z} - p_h^k (\phi_f)_h^k - (\Gamma_{opx})_h^k, \quad (3.11)$$

where $(\Gamma_{opx})_h^k$ is Γ_{opx} evaluated on the grid points.

It is how the residual (3.11) is chosen to vanish that distinguishes the two schemes. Horizontally, the collocation approach simply requires the residual to vanish on the grid points. That is,

$$\text{For all } (j, k) : R_h^k(x_i, z_j^k, t) = 0, \quad 1 \leq i \leq M. \quad (3.12)$$

Vertically, the Galerkin method requires the residual is L^2 -orthogonal to the solution basis V_N^k of polynomials of degree N whose support lies in element I^k . The DG interpolating polynomials span this basis:

$$V_N^k = \left\{ l_j^{DG,k} : 0 \leq j \leq N \right\}, \quad k = 1, 2, \dots, K. \quad (3.13)$$

This orthogonality condition is enforced by multiplying the residual by a test function from V_N^k and integrating. For each horizontal point x_i , we require

$$\int_{I^k} R_h(x_i, z, t) l_j^{DG,k}(z) dz = 0, \quad 0 \leq j \leq N, \quad 1 \leq k \leq K. \quad (3.14)$$

Integration by parts is performed twice on the flux terms in (3.14) for the strong DG form; suppressing h subscripts we write

$$\begin{aligned} \int_{I^k} \frac{\partial \phi_f^k}{\partial z} l_j^{DG,k} dz &\rightarrow - \int_{I^k} \phi_f^k \frac{\partial l_j^{DG,k}}{\partial z} dz + \int_{\partial I^k} (\phi_f^k)^* l_j^{DG,k} dz \\ &\rightarrow \int_{I^k} \frac{\partial \phi_f^k}{\partial z} l_j^{DG,k} dz + \int_{\partial I^k} \left((\phi_f^k)^* - \phi_f^k \right) l_j^{DG,k} dz. \end{aligned} \quad (3.15)$$

There are no continuity requirements on the solution across element boundaries, from which the discontinuous label in the method name originates. Rather, information is transferred across elements via the numerical flux $(\phi_f^k)^*$, which approximates ϕ_f^k on element boundaries. This flux is a consistent, monotone, Lipschitz-continuous function of all its arguments.

Applying the FC scheme (3.12) and DG scheme (3.14)-(3.15), the semi-discrete form of the porosity evolution equation (2.1) is

$$\begin{aligned} \frac{d\phi_f^k}{dt} = & -\frac{\gamma}{\delta} \mathcal{D}^{z,k} \phi_f^k \\ & + \frac{\gamma}{\delta} (\mathcal{M}^k)^{-1} \left[l_j^{DG,k} \left(\phi_f^k - (\phi_f^k)^* \right) \right]_{j=0}^{j=N} \\ & + p^k \phi_f^k + \Gamma_{opx}^k. \end{aligned} \tag{3.16}$$

The local mass and differentiation matrices, \mathcal{M}^k and $\mathcal{D}^{z,k}$, are defined as

$$\left(\mathcal{M}^k \right)_{m,n} = \int_{I_k} l_m^{DG,k} l_n^{DG,k} dz, \quad \left(\mathcal{D}^{z,k} \right)_{m,n} = \left. \frac{dl_n^{DG,k}}{dz} \right|_{z=z_m^k}, \tag{3.17}$$

and operate on solution columns via matrix-matrix products. The remaining products are computed by entry-wise multiplication. Using notation (3.9), the interpolant $l_j^{DG,k}$ takes the value 1 on all entries in row j and 0 elsewhere. At the cell intersection $I_k \cap I_{k+1} = [z_N^k, z_0^{k+1}]$ we use an upwinding numerical flux,

$$\left(\phi_f^k \right)^* = \phi_f^k \left(\cdot, z_N^k \right). \tag{3.18}$$

The opx evolution equation (2.2) is discretized in a similar fashion,

$$\begin{aligned} \frac{d\phi_{opx}^k}{dt} = & -\frac{\gamma}{\delta} \mathcal{D}^{z,k} \phi_{opx}^k \\ & + \frac{\gamma}{\delta} (\mathcal{M}^k)^{-1} \left[l_j^{DG,k} \left(\phi_{opx}^k - (\phi_{opx}^k)^* \right) \right]_{j=0}^{j=N} \\ & - \phi \Gamma_{opx}^k. \end{aligned} \tag{3.19}$$

As before, the numerical flux is computed by upwinding. Note that evaluation of the reaction rate Γ_{opx}^k in (3.16) and (3.19) involves computing the derivative $\partial p / \partial z$, for which we apply the DG derivative.

Lastly, the elliptic equation (2.4) is a modified Helmholtz equation, discretized by introducing the auxiliary variable $q = \partial p / \partial z$ to reduce the equation into a system of first order equations. To accommodate the non-zero Dirichlet boundary condition $p(z=0) = p_0$, we substitute $p = \hat{p} / \delta + p_0$ so that $\hat{p}(z=0) = 0$, yielding a modified right hand side $g = -\delta p_0 \phi_f - \partial \phi_f^3 / \partial z$ to (2.4). The local discretization becomes

$$\begin{aligned} -\mathcal{M}^{z,k} \left[\left(\phi_f^{k^3} \left(\hat{p}^k (\mathcal{D}^x)^T \right) \right) (\mathcal{D}^x)^T + \mathcal{D}^{z,k} \left(\phi_f^{k^3} q^k \right) - \hat{p}^k \phi_f^k \right] \\ + \left[l_j^{DG,k} \left(q^k - (q^k)^* \right) \right]_{j=0}^{j=N} = \mathcal{M}^{z,k} g^k, \end{aligned} \tag{3.20a}$$

$$q^k = \mathcal{D}^z \hat{p}^k - \left(\mathcal{M}^{z,k} \right)^{-1} \left[l_j^{DG,k} \left(\hat{p}^k - (\hat{p}^k)^* \right) \right]_{j=0}^{j=N}. \tag{3.20b}$$

Horizontal derivatives are computed with the Fourier differentiation matrix D^x as given in (3.4).

For the numerical fluxes $(\hat{p}^k)^*$ and $(q^k)^*$ we use a stabilized central flux [2], generally given on the intersection of cells $I_k \cap I_{k+1} = [z_N^k, z_0^{k+1}]$ as

$$(\hat{p})^* = \{\{\hat{p}\}\}, \quad (3.21a)$$

$$(q)^* = \{\{q\}\} - \tau[\hat{p}], \quad (3.21b)$$

where $\{\{u\}\} = 1/2(u(\cdot, z_N^k) + u(\cdot, z_0^{k+1}))$ is the average solution at the cell interface while $[u] = u(\cdot, z_0^{k+1}) - u(\cdot, z_N^k)$ is the jump across the interface. τ is a positive number, whose role is to penalize jumps in \hat{p} . Different values of τ affect the accuracy of the scheme and conditioning of the linear system; greater discussion and analysis can be found in [8]. We select $\tau = 1$. Boundary conditions are enforced through the numerical flux by setting $\hat{p}(z_N^0) = -\hat{p}(z_0^1)$ and $q(z_0^{K+1}) = q(z_N^K)$.

Assembling (3.20) over all DG elements, we are left to solve a linear system of size D -by- D , where $D = (N+1) \times K \times M$. This system is nonsymmetric due to the permeability ϕ_f^3 . As a solver, we use a matrix-free implementation of the BiCGStab iterative method [10]. Solving the Helmholtz equation is the main bottleneck in computation.

Finally, we note that with a nodal DG scheme, integrals are computed via quadrature on the $N+1$ Gauss-Lobatto grid points, which is exact for polynomials up to order $2N-1$. For higher-order, nonlinear terms that exceed this order, aliasing errors may lead to numerical instability. A standard, robust way to maintain stability is to post-process solutions at each time step with a filter (equivalent to adding artificial dissipation [8]). To this end, we apply an exponential filter on the porosity in both the vertical and horizontal dimensions. This in effect damps only the highest solution modes, and retains accuracy while preventing numerical instability. Implementation details for such a filter can be found in [7] and [8].

3.3 Convergence study

The efficiency of a high-order method is apparent when considering the relatively rapid rate of convergence. We expect exponential decay in the approximation error with increasing solution orders M and N , and polynomial decay in the approximation error with increasing number of DG elements K . This is demonstrated in Fig. 1

To verify the convergence of the FC scheme we conduct transient simulations of (2.1)-(2.5) with standard parameter choices on a domain width $x_{\max} = 1$ with the boundary condition $\phi_f(x, z = 0, t) = 1 + 0.05 \exp[-100(x - 0.5)^2]$ and take the vertical extension of this throughout the domain as an initial condition. This setup guarantees a smooth transient solution with energy in all representable horizontal wavenumbers. We conduct simulations with varying number of M horizontal grid points up to a terminal time $t = 0.5$, with 6 DG elements of order 10 in the vertical dimension. As an ‘‘exact’’ solution, we choose

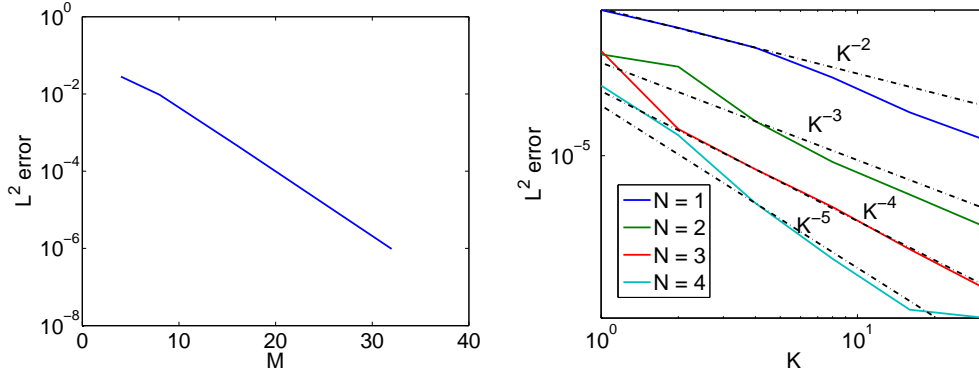


Figure 1: Convergence study. L^2 error rates in porosity ϕ_f are shown. The error decays exponentially as a function of FC order M and DG order N , and polynomially as a function of element size K^{-1} . Dashed black lines in right panel denote reference lines of slope $K^{-(N+1)}$.

a well-resolved case of $M = 128$. In Fig. 1 it is seen that the L^2 -error decays exponentially as a function of M , verifying spectral convergence of the scheme.

To verify the convergence of the DG scheme we take the same parameter and domain setup as in the previous case, and assume exact, steady solutions

$$\phi_f^e(x, z) = \exp(0.04z) (1 + 0.1 \cos(2\pi x)), \tag{3.22}$$

$$p^e(x, z) = (p_0 + 0.1 \cos(2\pi x)) z \sin(0.75\pi z) + 0.1 z \cos(2\pi x). \tag{3.23}$$

Substituting (3.22)-(3.23) into (2.1) and (2.4) yields a residual for each equation that is in turn added back to the equations, guaranteeing an exact solution as prescribed. We integrate this system to steady state with very small time steps. From general analysis of the DG method [8] we expect the error of the scheme to diminish as a polynomial function of the size of the element, K^{-1} . This is confirmed in Fig. 1, where it is seen that the L^2 -error decays as $K^{-(N+1)}$. Moreover, exponential convergence is observed as a function of the DG order N .

4 Linear stability analysis of the physical system

We will use a linear stability analysis of the non-dimensionalized equations (2.1)-(2.6) to verify the results of our discretization and to gain insight into the dynamical behavior of the system. In [6] this analysis is described in depth; the numerical discretization used in this analysis is discussed here. We assume $z_{\max} = 0.75z^*$, computed in Eq. (2.9). Observing that the opx abundance evolution equation (2.2) is decoupled from the melt evolution (2.1) and compaction rate (2.4) equations, we may consider the simpler two-variable $u \in \{\phi_f, p\}$ system. Accordingly, we linearize each around the one-dimensional base states (2.8)

$$u(x, z, t) = \bar{u} + \epsilon \tilde{u} e^{ikx + \sigma t}, \tag{4.1}$$

where $\epsilon \ll 1$ is a small number, and $k \in [0, \infty)$ is the horizontal perturbation wavenumber. We seek eigenpairs $(\sigma, \tilde{u}(z))$ representing the dominant growth rate and vertical solution mode, respectively. The boundary conditions on the perturbations are

$$\tilde{\phi}_f(0) = \tilde{p}(0) = \left. \frac{\partial \tilde{p}}{\partial z} \right|_{z=z_{\max}} = 0. \tag{4.2}$$

Substituting (4.1) into (2.1), (2.4), and (2.5), and keeping only $O(\epsilon)$ terms results in the linear system

$$\begin{pmatrix} A_{S\phi_f} & A_{Sp} \\ A_{P\phi_f} & A_{Pp} \end{pmatrix} \begin{pmatrix} \tilde{\phi}_f \\ \tilde{p} \end{pmatrix} = \sigma \begin{pmatrix} 1 & 0 \\ 0 & 0 \end{pmatrix} \begin{pmatrix} \tilde{\phi}_f \\ \tilde{p} \end{pmatrix} \tag{4.3}$$

with entries

$$A_{S\phi_f} = -\frac{\gamma}{\delta} \mathcal{D} + \bar{p} - \frac{\gamma - 3\bar{\phi}_f^2(\delta\bar{p}' - 1)}{\delta z - 1}, \tag{4.4a}$$

$$A_{Sp} = \bar{\phi}_f - \frac{\delta\bar{\phi}_f^3}{1 - \delta z} \mathcal{D}, \tag{4.4b}$$

$$A_{P\phi_f} = \delta\bar{p} - 3 \left[(\delta\bar{p}' - 1) \left(\bar{\phi}_f^2 \mathcal{D} + (\bar{\phi}_f^2)' \right) - \delta\bar{\phi}_f^3 \bar{p}'' \right], \tag{4.4c}$$

$$A_{Pp} = \delta \left[\bar{\phi}_f - 3\mathcal{D}\bar{\phi}_f\bar{\phi}_f^2 + (k^2 - \mathcal{D}^2)\bar{\phi}_f^3 \right]. \tag{4.4d}$$

The \mathcal{D} operator is the (discontinuous Galerkin) derivative, comprised of the local differentiation matrix and numerical flux terms,

$$\mathcal{D} = \mathcal{D}^{z,k} + (\mathcal{M}^k)^{-1} \left[l_j^{DG,k} (u^k - (u^k)^*) \right]_{j=0}^{j=N}. \tag{4.5}$$

Note that the numerical flux $(u^k)^*$ varies depending upon whether one is computing the derivative of ϕ_f (upwinding) or p (central). Substituting $\tilde{p} = -(A_{Pp})^{-1} A_{P\phi_f} \tilde{\phi}_f$ into the generalized eigenvalue problem (4.3) reduces the system to the standard eigenvalue problem

$$\left(A_{S\phi_f} - A_{Sp} A_{Pp}^{-1} A_{P\phi_f} \right) \tilde{\phi}_f = \sigma \tilde{\phi}_f. \tag{4.6}$$

Eigenpairs $(\sigma, \tilde{\phi}_f)$ are easily computed from the linear system (4.6) with standard methods.

The DG method is a highly effective tool in stability analysis computations for a variety of reasons. For one, the high-order solution approximation allows for accurate resolution of oscillatory eigenfunctions. Furthermore, the combination of element order or size (N or K) refinement allows for efficient computation of eigenpairs with far fewer degrees of freedom than a low-order scheme would allow, thereby improving the conditioning of the left-hand-side operator in (4.6). This latter point alludes to the robustness of the

DG method in computing dispersion relationships, specifically in avoiding convergence to spurious (nonphysical) modes. In practice, this is a concern for high wavenumber k . For greater discussion of the spectral properties of discontinuous Galerkin operators we refer to [8].

4.1 Two unstable regimes: channels and waves

In [6], stability of our model system is explored over $\gamma - \delta$ space, and it is observed that two distinct types of instability (i.e. $\text{Re}(\sigma) > 0$) occur. We will refer to these as the “channel” and “wave” regimes, corresponding to the case of $\text{Im}(\sigma) = 0$ and $\text{Im}(\sigma) \neq 0$, respectively. These names are motivated by the structure of the computed eigenfunction $\tilde{\phi}_f$ and the nature of the time-dependent behavior of the solution. Key observations from [6] include a boundary in $\gamma - \delta$ space separating these instabilities to be a function of the ratio γ/δ^2 , as well as the existence of a stable regime sandwiched between the two unstable regimes that diminishes with decreasing φ .

In Fig. 2 we examine results from the linear stability analysis with two different upwelling rates, $\gamma \in \{10^{-5}, 10^{-2}\}$. It is observed that with little upwelling, the growing solution modes are monotonic in z and the dispersion relationship does not yield a preferred wavenumber. In this case, the computed eigenvalue is purely real, so small perturbations are expected to grow monotonically in time as well. However, in the case of moderately higher upwelling rate, the computed eigenfunctions are now oscillatory in z , and the eigenfunctions have a nonzero complex part. Consequentially, a wave-like variation in time is predicted. A peak in the dispersion relationship in the neighborhood of $k = 4.5$ indicates a preferred wavenumber for the given parameter settings. We restrict further numerical study to the wave regime case, as this value of γ is more relevant to our physical setting.

4.2 Diagnosing oscillatory growth or decay

Before continuing with stability analysis we introduce an algorithm that allows one to diagnose oscillatory growth or decay from transient solution sets. In this way, we may match results from analysis to what is actually observed in numerical simulation. In [4] it is shown that simple recurrence relationships may be used to compute the linear behavior of a signal

$$f_n \simeq \exp[(\alpha + i\omega)n\Delta t]. \tag{4.7}$$

The signal f_n is sampled at equally spaced time intervals Δt . Quantities r^2 and $2x$ are defined as

$$r^2 = \frac{f_{n+2}f_n - f_{n+1}^2}{f_{n+1}f_{n-1} - f_n^2}, \tag{4.8}$$

$$2x = \frac{f_{n+2}f_{n-1} - f_{n+1}f_n}{f_{n+1}f_{n-1} - f_n^2}. \tag{4.9}$$

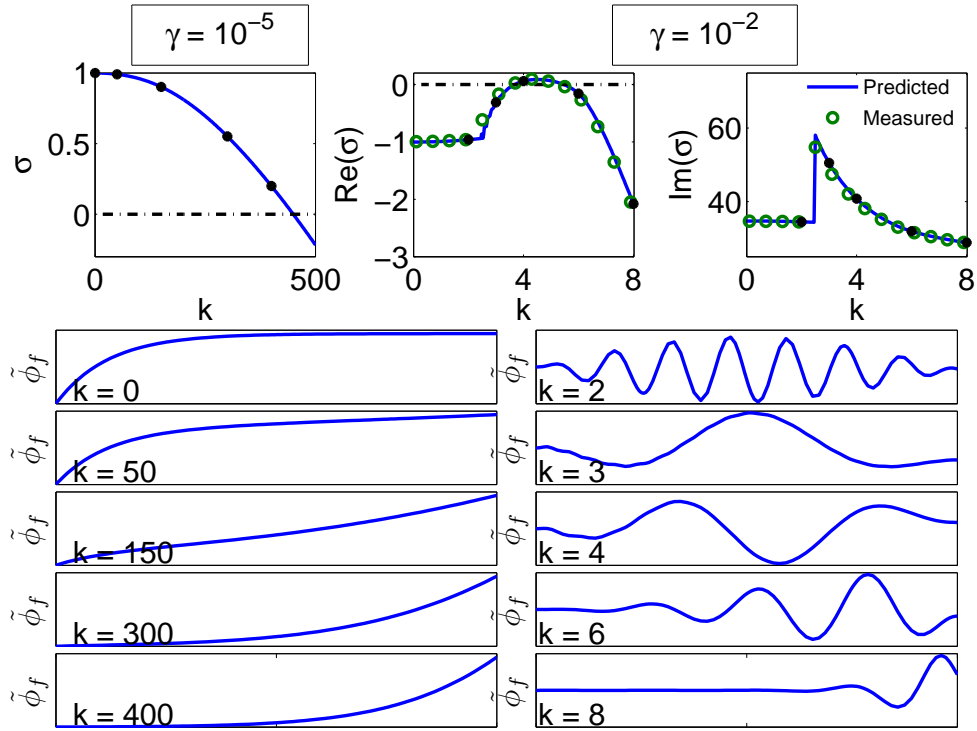


Figure 2: Results from linear stability analysis (4.3)-(4.4). Two upwelling rates, $\gamma \in \{10^{-5}, 10^{-2}\}$, are compared. With smaller upwelling, eigenfunctions are monotonic, eigenvalues are purely real, and there is no preferred wavenumber selection. With greater amounts of upwelling, eigenfunctions are oscillatory, eigenvalues are complex, and a peak in the dispersion relationship reveals a strong wavenumber selection. Transient simulations from our numerical model are verified to match the behavior predicted by linear analysis.

Values for the real numbers α and ω , the growth rate and frequency, respectively, are then given as r^2 and $2x$ converge,

$$\gamma = \frac{1}{2\Delta t} \log r^2, \tag{4.10}$$

$$\omega = \frac{1}{2\Delta t} \cos^{-1} \left(2 \frac{x^2}{r^2} - 1 \right). \tag{4.11}$$

We extend the method of [4] to extract the numerical growth rate and angular frequency from transient simulations seeded with the dominant eigenfunction (numerically computed for each k),

$$\phi_f(x, z, t=0) = \bar{\phi}_f + 0.01 \tilde{\phi}_f \cos(kx). \tag{4.12}$$

A horizontal domain length x_{\max} is selected to ensure periodicity of wavenumber k . Solutions are then computed with our numerical scheme up to a terminal time $t = 1$, taking equal time steps. To reduce the two-dimensional ϕ_f field to a single “signal” data point f_n , at each time step we do the following:

1. Subtract the base state $\bar{\phi}_f$, to achieve an (approximately) zero-mean solution.
2. Extract the energy $E_k(z)$ in the k -mode at each vertical level by taking the FFT across the horizontal dimension.
3. Integrate E_k over z .

4.3 Verification of numerical discretization

Beyond predicting to first order the dynamic behavior of the nonlinear system, the linear stability analysis in Section 4 also provides a mechanism to verify our discretization, so long as the solution fields are relatively close to the steady states given in Eq. (2.8). This is accomplished in the following manner: selecting a horizontal wavenumber perturbation k , we compute the eigenfunction $\tilde{\phi}_f$ and evolve the initial condition

$$\phi_f(x, z, 0) = \bar{\phi}_f + 0.01\tilde{\phi}_f \cos(kx). \quad (4.13)$$

A horizontal domain length $x_{\max} = 2 * 2\pi / k$ is chosen to ensure resolution of the given wavenumber. With the data stored from each time step we compute the (numerical) growth rate and angular frequency, using recurrence relationships (see [4], and Section 4.2). These numerical values are then compared to the predicted values, $\text{Re}(\sigma)$ and $\text{Im}(\sigma)$, respectively. In Fig. 2 this comparison is demonstrated for the standard case $\gamma = 10^{-2}$ over wavenumbers $0 \leq k < 8$. Numerical growth and angular frequency rates are computed at the terminal time $t=1$. Our numerical discretization is very well matched to the predicted behavior.

Next, we employ the numerical scheme to verify the preferred wavenumber trend evidenced by the peak in the dispersion relationship from Fig. 2. This is accomplished by evolving the initial condition

$$\phi_f(x, z, 0) = \bar{\phi}_f + 0.1\tilde{\phi}_{f,2} \cos(2x) + 0.01\tilde{\phi}_{f,4} \cos(4x), \quad (4.14)$$

where $\tilde{\phi}_{f,2}$ and $\tilde{\phi}_{f,4}$ are the computed eigenfunctions from the $k=2$ and $k=4$ horizontal wavenumber perturbations, respectively (displayed in Fig. 2). Whereas $\tilde{\phi}_{f,2}$ is seeded with ten times the perturbation magnitude of $\tilde{\phi}_{f,4}$ we expect from the linear stability analysis the former to decay and the latter to grow exponentially in time. This transition (from wavenumber 2 to 4) is presented in Fig. 3. With a horizontal domain length $x_{\max} = 2\pi$, two wave crests are dominant in the initial ϕ_f field. Stepping forward in time, we observe a transition to four wave crests by time $t=5$.

As a means of quantifying this transition, we compute the expected value $\langle k \rangle$ of the wavenumber,

$$\langle k \rangle = \sum_k k \frac{\int_0^{z_{\max}} |E_k|^2 dz}{\sum_k \int_0^{z_{\max}} |E_k|^2 dz}, \quad (4.15)$$

where E_k are the discrete Fourier coefficients of the zero-mean quantity $\phi_f - \bar{\phi}_f$ and are easily computable via the FFT. The quantity $|E_k|^2$ is a measure of energy in wavenumber

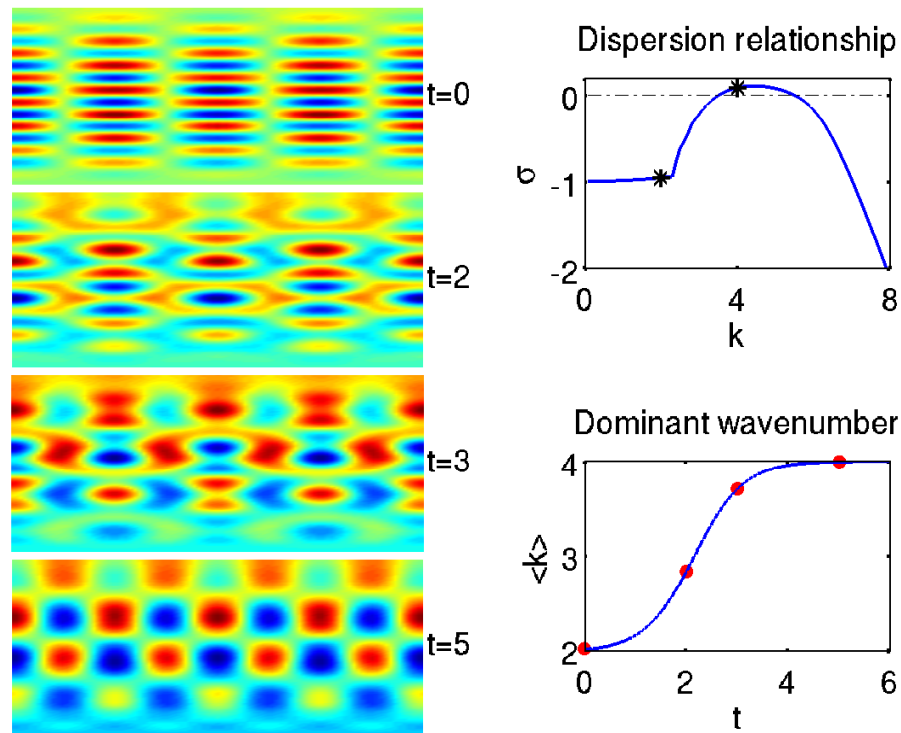


Figure 3: Wavenumber selection. Initially most of the energy is focused in the stable $k=2$ mode, with a small amount in the unstable $k=4$ mode. As predicted by linear stability analysis, the former decays while the latter emerges as the dominant feature.

k , and the fractional quantity in (4.15) acts as a discrete probability density. Plotted in Fig. 3 as a function of time, $\langle k \rangle$ smoothly transitions from the initially seeded $k=2$ to the preferred $k=4$.

5 Results from numerical simulations

Linear stability analysis provides a foundation from which we may begin to explore non-linear behavior of our model, yielding locations in parameter space that are conducive to physical instability. Here we present a few results from transient simulations of our numerical scheme.

5.1 Simulating the effects of mantle heterogeneity with a fixed boundary perturbation in porosity

While the linear stability analysis presented in Section 4 measures the response of the system to small, internal perturbations, we also observe interesting dynamical behavior in response to altering the inflow porosity boundary condition. Consider the evolution

of the IBVP (2.1)-(2.6) with initial values $\phi_f = \bar{\phi}_f, \phi_{opx} = \bar{\phi}_{opx}$, and modifying the porosity boundary condition as

$$\phi_f(x,0,t) = 1 + A \exp \left[-50(x/x_{\max} - 0.5)^2 \right], \quad A > 0. \quad (5.1)$$

We select a domain width $x_{\max} = 1$ and height $z_{\max} = 0.75z^* \approx 2.69$ (Eq. (2.9)). The chosen width admits a minimum resolvable horizontal wavenumber of $k = 2\pi$, placing us in a regime stable to internal perturbation (Fig. 2). Therefore we expect a steady-state solution to exist. Generally, an aspect ratio in the range

$$x_{\max}/z_{\max} \in [0.5, 1] \quad (5.2)$$

is adequate to resolve simulations with porosity inflow perturbations as prescribed by Eq. (5.1). This is confirmed by comparing the far-field solutions to the one-dimensional base state (e.g. $\phi_f(0,z,t)$ and $\bar{\phi}_f(z)$, respectively).

Fig. 4 presents results with the sustained boundary perturbation in porosity (5.1). From left to right, ϕ_f (top) and ϕ_{opx} (bottom) are presented for increasing amplitudes $A = \{0.05, 0.1, 0.2, 0.4\}$. We use $K = 10$ equally spaced DG elements of order $N = 6$, and $M = 120$ horizontal grid points. Transient simulations are performed until a terminal time $t = 3$, at which time steady state has been reached. A number of observations can be made from these simulations. The fixed porosity boundary perturbation induces multiple melt channels (top row) and a single dunite channel (bottom row). The channel of melt bifurcates as a consequence of opx exhaustion. Larger perturbation amplitudes deepen the depth of the dunite channel. Compacting (i.e. low-porosity) boundary layers are observed outside high-porosity melt channels. Greater analysis of these observations and discussion as to their geological consequences is given in [11].

In Fig. 5 we consider a mesh refinement study for the case $A = 0.2$ from Fig. 4. We fix the DG element order $N = 6$, as numerical experiments yield this to be a robust value for attaining high-order accuracy while still allowing for a large explicit time step to be taken. From left to right, ϕ_f (top) and ϕ_{opx} (bottom) are presented for resolutions of $(K=10, M=60)$, $(K=10, M=120)$, and $(K=20, M=320)$. For the coarsest resolution (left-most column), we see numerical oscillations in the bifurcated melt channels. These are due to the smearing of the dunite channel interface. With increasing resolution, these oscillations disappear. Although fine resolution is needed to resolve the thin melt channels in ϕ_f , we observe that ϕ_{opx} appears well-resolved for even the coarsest resolution.

5.2 Interaction between channels and waves

Linear analysis of the problem predicts porosity waves (Fig. 2), and we have observed that a sustained boundary perturbation in the inflow melt fraction induces a channel of melt that bifurcates upon exhaustion of the opx abundance (Fig. 4). Next we consider the superpositioning of these effects, by conducting numerical experiments in the wave regime with a fixed boundary perturbation.

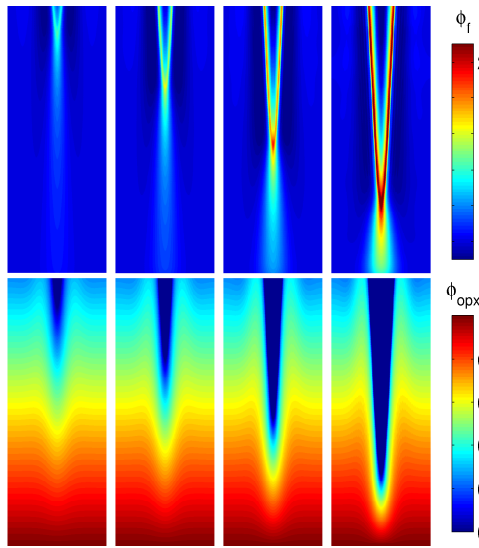


Figure 4: Steady-state solutions with sustained inflow porosity perturbation as given in (5.1). Top: fluid fraction. Bottom: opx abundance. From left to right, perturbation amplitude $A = \{0.05, 0.1, 0.2, 0.4\}$.

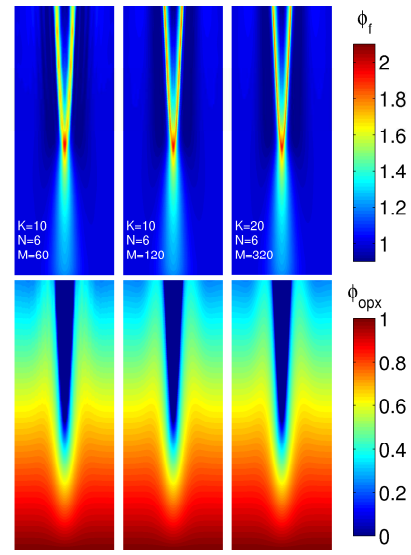


Figure 5: Convergence study, using same setup as case $A=0.2$ in Fig. 4. From left to right, we use resolutions of $(K=10, M=60)$, $(K=10, M=120)$, and $(K=20, M=320)$. The DG order is taken as $N=6$. In the coarsest resolution we see numerical oscillations in the melt channels; these disappear with refinement.

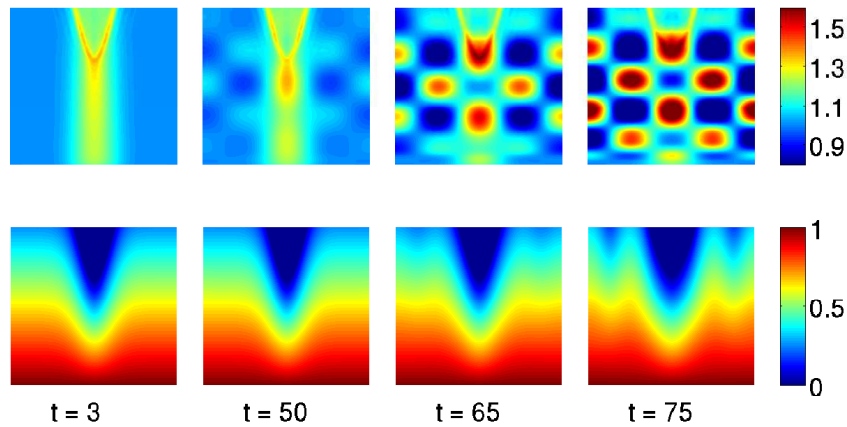


Figure 6: Evolution of fluid fraction (top) and opx abundance (bottom) in unstable wave regime with fixed boundary perturbation (5.1). Interaction between porosity waves, inherent to the system, and a central channel, induced by the boundary condition, is observed. Outflow dunite (opx-free) channels are shown to vary in time as strong porosity waves emerge.

In Fig. 6 we show results from a simulation with the fixed inflow perturbation in porosity as prescribed by Eq. (5.1), although now we select a horizontal domain width $x_{\max} = 4\pi/4.4 \approx 2.86$. This suffices to guarantee a physical instability that is representable

with our numerical scheme. We use $K = 10$ equally spaced DG elements of order $N = 6$, and $M = 80$ horizontal grid points. Results are shown starting at time $t = 3$, from which the initial effects of the boundary perturbation have fully evolved. At $t = 50$, wave features are noticeable in the porosity field. These amplify with time, shown later at $t = 65$ and $t = 75$, eventually overwhelming the channel. The waves induce secondary high-porosity regions, locally increasing the reaction rate ($\Gamma_{opx} \sim \phi_f^3$, per Eq. (2.5)) and thus creating secondary dunite channels.

5.3 Dependence upon horizontal domain size

With the assumption of periodic boundary conditions, the domain length x_{\max} is the largest representable wavelength in the horizontal dimension; in other words, we are constrained in which wavenumbers we are able to represent. With M grid points, the observable wavenumbers are quantized into units $2\pi n / x_{\max}$, with integer $n \leq M/2$. This is clearly an issue to be recognizant of when performing long-time integration, where predictions from linear theory are not necessarily valid.

To demonstrate this we consider a series of numerical experiments with varying domain sizes $x_{\max} = n * 2\pi / 4.4, n \in \{4, 5, 6\}$ and a small-amplitude noisy initial input with energy in all representable wavenumbers. The inflow porosity boundary condition is fixed as $\phi_f(x, 0, t) = 1$. We use $K = 2$ equally spaced DG elements of order $N = 12$, and $M = 40$ horizontal grid points. Although this is a coarser mesh than simulations in Figs. 4 and 6, it is sufficient for this simpler setting where there is no sustained constant inflow boundary condition with only a small amplitude initial perturbation. Similar to Fig. 3,

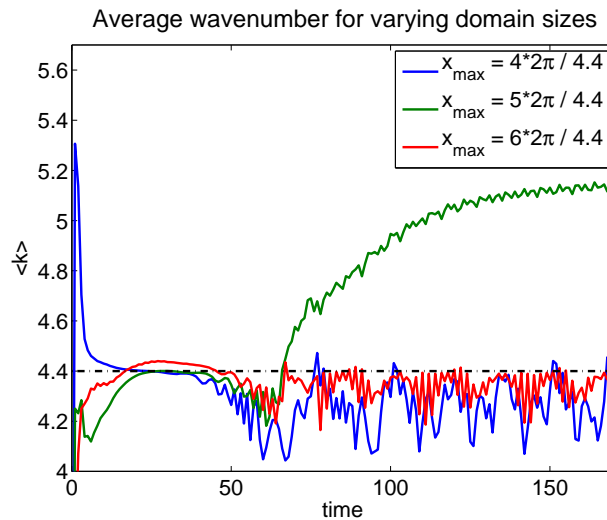


Figure 7: Expected wavenumber $\langle k \rangle$ as a function of time for varying horizontal domain length x_{\max} . The assumption of periodic boundary conditions constrains which wavenumbers we are able to represent.

the preferred wavenumber is initially selected according to linear theory. However, for $n = 5$ we observe a transition at later times to the next representable wavenumber.

5.4 Comparison to previous results

Previous numerical study of a similar system was presented in [13], although with a slightly different model than the one presented. These differences include no solid upwelling (i.e., $\gamma = 0$), no explicit tracking of opx abundance (Eq. (2.2) of the present study), a bulk viscosity independent of porosity (i.e., $p\phi_f$ becomes p in Eqs. (2.1) and (2.4)), and local chemical disequilibrium (see Eqs. (3) and (4) in [13]). Moreover, the present study neglects diffusion and dispersion in the melt (i.e., Peclet number $Pe = \infty$ in the notation of [13]).

Despite these differences, comparisons between the two models are still possible. Because [13] includes no solid upwelling, the compaction-porosity waves we observe in Figs. 2, 3, and 6 are not observed in [13]. Rather, all simulations in [13] occur in the dynamically unstable “channel” regime. Melt channel bifurcation (Figs. 4 and 6) is not observed in [13], as this feature is a consequence of opx depletion. A semi-analytic solution to the stability analysis detailed in Section 4 is given in [6], and demonstrates that a porosity-dependent bulk viscosity stabilizes the system, linearly decreasing the growth rate of an infinitesimal perturbation. Transient numerical simulations in [11] demonstrate that the setting of local chemical equilibrium is the most dynamically unstable.

6 Summary

In this paper, a high-order numerical scheme has been presented for the equations of magma dynamics described by the physical models presented in [6, 11]. This model includes a porosity-dependent bulk viscosity term, a solid upwelling term and a hyperbolic equation to track the fraction of the dissolvable mineral opx. The latter quantity is used as a level set function, where upon exhaustion the mass transfer rate is taken to zero.

Our numerical implementation consists of a Fourier collocation method in the horizontal direction and a discontinuous Galerkin method in the vertical direction. Numerical error estimates match their theoretically expected values. A high-order method is well-suited to resolve the compaction-dissolution waves which are predicted by linear analysis. Our discretization is verified to match transient behavior predicted by linear stability analysis; a strong wavenumber selection is observed in the presence of moderate upwelling rate. In assuming periodicity in the horizontal dimension, we effect a length scale which may bias the wavenumber selection observed in transient simulations.

Transient numerical simulations reveal new insight into the full, nonlinear system. Mantle heterogeneity, represented by a perturbation in the inflow melt fraction, appears to be an agent of dunite channel formation. Compacting boundary layers are observed outside high-porosity melt channels. In the event of depleted opx abundance, melt channels bifurcate.

Acknowledgments

This work was supported in part by NSF grant DMS-0530862. The authors wish to thank Y. Liang and E. M. Parmentier for helpful discussion and suggestions.

References

- [1] E. Aharonov, J. Whitehead, P. B. Kelemen and M. Spiegelman, Channeling instability of upwelling melt in the mantle, *J. Geophys. Res.*, 100 (1995), 433-450.
- [2] D. N. Arnold, F. Brezzi, B. Cockburn and L. D. Marini, Unified analysis of discontinuous galerkin methods for elliptic problems, *SIAM J. Numer. Anal.*, 39 (2002), 1749-1779.
- [3] D. Bercovici, Y. Ricard and G. Schubert, A two-phase model for compaction and damage 1. General theory, *J. Geophys. Res.*, 106 (2001), 8887-8906.
- [4] O. Buneman, Diagnosing oscillatory growth or decay, *J. Comput. Phys.*, 29 (1978), 295-296.
- [5] M. H. Carpenter and C. A. Kennedy, Fourth-order 2N-storage Runge-Kutta schemes, NASA TM 109112, NASA Langley Research Center, 1994.
- [6] M. A. Hesse, A. R. Schiemenz, Y. Liang and E. M. Parmentier, Compaction-dissolution waves in an upwelling mantle column, *Geophys. J. Int.*, 2011 (submitted).
- [7] J. S. Hesthaven, S. Gottlieb and D. Gottlieb, *Spectral Methods for Time-Dependent Problems*, Cambridge University Press, 2006.
- [8] J. S. Hesthaven and T. Warburton, *Nodal Discontinuous Galerkin Methods: Algorithms, Analysis, and Applications*, Springer, 2008.
- [9] P. B. Kelemen, G. Hirth, N. Shimizu, M. Spiegelman and H. J. B. Dick, A review of melt migration processes in the adiabatically upwelling mantle beneath oceanic spreading ridges, *Phil. Trans. R. Soc. Lond.*, 355 (1997), 282-318.
- [10] Y. Saad, *Iterative Methods for Sparse Linear Systems* (2nd edition), SIAM Publishing, 2003.
- [11] A. R. Schiemenz, Y. Liang and E. M. Parmentier, A high-order numerical study of reactive dissolution in an upwelling heterogeneous mantle: I. Channelization, channel lithology, and channel geometry, *Geophys. J. Int.*, 2011. DOI: 10.1111/j.1365-246X.2011.05065.x (in press).
- [12] M. Spiegelman and P. B. Kelemen, Extreme chemical variability as a consequence of channelized melt transport, *Geochem. Geophys. Geosyst.*, 4(7) (2003), 1055.
- [13] M. Spiegelman, P. B. Kelemen and E. Aharonov, Causes and consequences of flow organization during melt transport: The reaction infiltration instability in compactible media, *J. Geophys. Res.*, 106 (2001), 2061-2077.